Wiley
International Journal of Energy Research
Volume 2025, Article ID 6804808, 8 pages
https://doi.org/10.1155/er/6804808

WILEY

Research Article

Performance Analysis of a Novel Lead-Free Monolithic Perovskite/Silicon Tandem Solar Cell Using SCAPS-1D

Rachna Singh,[1] **Alok Joshi**,[1] **and Gunjan Gupta**[2]

[1]*Department of Electronics and Communication Engineering, Jaypee Institute of Information Technology, Noida, Uttar Pradesh, India*
[2]*Department of Electrical, Electronics and Communication Engineering, Cape Peninsula University of Technology, Bellville, South Africa*

Correspondence should be addressed to Gunjan Gupta; guptag@cput.ac.za

Received 9 June 2025; Revised 13 October 2025; Accepted 21 October 2025

Academic Editor: Ahmad Azmin Mohamad

In solar cells, efficiency is the most critical parameter. In single-junction solar cells, efficiency is always limited, so to increase the efficiency beyond a specific range, we need to switch to a tandem configuration. Tandem configuration is the stacking of two different cells together, termed as top and bottom cells, where the electrical properties of these two cells are different. ln this paper, free perovskite material with a wide band gap of 1.5 eV ($CsSnGeI_3$) is used to make the top cell, and a narrow band gap of 1.12 eV crystalline silicon is used to create a bottom cell. The advantage of using perovskite material is its high light conversion rate, which leads to better efficiency. Power conversion efficiency (PEC) for perovskite cells is up to 30%. The proposed cell is simulated by SCAPS-1D. In this process, the top and bottom cells are calibrated in the standalone conditions before analyzing the tandem configuration, where the optimized thickness for the top cell is 100 nm and that of the bottom cell is 200 nm. To combine both cells, the current of both cells should be matched, where the top cell current acts as a limiting factor. By changing the width of the top cell for a filtered spectrum and integrated filtered power, a matched current of 18.34 mA cm^{-2} is obtained for the top/bottom cell. The resultant parameters of the proposed tandem solar cell are PCE of approximately 26%, open circuit voltage (V_{oc}) of 1.576 V, fill factor (FF) of 90%, and short circuit current (J_{sc}) of 18.34 mA cm^{-2}. The proposed device can help develop low-cost applications and high-efficiency tandem solar cells.

Keywords: monolithic; perovskite; SCAPS-1D simulation; tandem solar cell

1. Introduction

The development of perovskite material ($CH_3NH_3PbX_3 = Cl$, Br, I) in manufacturing solar cells has significantly impacted third-generation solar cells [1, 2]. The perovskite material significantly increases the power conversion efficiency (PCE), that is, up to 24% [3]. However, the main challenge with these materials is lead toxicity, as one of the main ingredients in perovskite materials is lead, which adversely affects the environment. This drawback can be overcome by switching to tin (Sn)-based perovskite materials like $MASnI_3$ ($CH_3NH_3SnI_3$) [4]. These Sn-based perovskite materials have been used as a lead-free substitute with a planar heterojunction design [5]. The stability of organic-based methyl ammonium (MA) and formamidinium (FA) perovskites is low, which has led to alternative materials like Cs-based cation perovskite [6]. The challenges posed by lead-free perovskite materials underscore the need for further research and innovation in this area.

Another disadvantage of Sn-based solar cells is that they have Sn^{2+} and Sn^{4+}, which oxidize very quickly when exposed to air and increase the instability in Sn-based solar cells. Sn can be replaced by lead easily, as they are the same group members in the periodic table, and stability can be increased, but again, lead will have adverse effects on the environment. All these disadvantages have been overcome by a material proposed by Chen et al. [7], where $CsSnI_3$ has been alloyed with Ge^{2+} to

create a stable and air-tolerant $CsSn_{0.5}Ge_{0.5}I_3$ perovskite structure. Chen et al. [7] introduced a perovskite absorber material, $CsSnGeI_3$, which exhibits better performance and remarkable air stability than its pure forms, CsSnI3 and CsGeI3. The device utilizing $CsSnGeI_3$ achieved a PCE of 7% [8]. The above structure is used in this work to make the top cell. The stability of the above-mentioned solar cells increases significantly due to their structure, which consists of an octahedral factor of 0.4 and a Goldschmidt tolerance factor of 0.94 [7]. There is one more alternative to Sn-based perovskite material: we can increase its stability by adding SnF_2, which will reduce oxidation [9]. The solar cells made up of SnF_2–based materials have shown stability for more than 100 days without reducing the efficiency, that is, 98% efficiency can be achieved [5]. A thorough understanding of material properties and device architecture should be there to increase the performance of $CsSn_{0.5}Ge_{0.5}I_3$-based devices.

The maximum achievable efficiency of solar cells with a single junction has been constrained to 33%, as stated in the *S-Q* limit, a mathematical expression given by Hans-Joachim Queisser and William Shockley in 1961 [3]. This limits maximum output through a single-junction solar cell, as the complete utilization of the sun's spectrum is impossible. Numerous cells with different bandgaps can be stacked together to overcome this drawback. Cells with different bandgaps will help absorb photons from various bands, which results in maximum utilization of the sun spectrum, and sequentially, the output of these cells increases. The resultant device is a tandem device with different bandgap subcells stacked together to form a tandem configuration. Its architecture consists of mechanically stacked layers integrated monolithically and spectrally split. The above device can be grouped as 2T (two terminals), 3T, and 4T according to how these subcells are connected,that is, whether they are in series or parallel [4]. Apart from increasing efficiency, the tandem devices reduce optical (thermalization) and electrical (transmission) losses. The proposed research has simulated monolithic PVSK/silicon tandem solar cells because both layers work efficiently together. The silicon layer can efficiently convert the infrared component of sunlight into electrical energy, while the perovskite layer uses the visible range of solar power [9]. This happens because of the molecular formula of perovskite material, that is, ABX_3, where X is a halide (Br, I, or F) and A/B are distinct cations [6]. In 2015, the first tandem solar cell came into existence with a PCE of 13.7% [10]. The efficiency of the above solar cell was reduced due to less photocurrent. As the efficiency of the perovskite material is much higher than that of other materials used for manufacturing solar cells, this has resulted in PSVK/Si tandem solar cells, where the efficiency has increased to 25.6% [11]. This elevated performance of perovskite material has resulted in PVSK/Si tandem solar cells whose PCE has increased up to 29.15%, as shown in the state of the art [12]. Apart from higher efficiency, 2T tandem devices have lower fabrication costs and parasitic losses, as only one transparent conducting electrode is needed in designing them. If we introduce defects in device simulation, its performance will be affected. The device performance is inversely proportional to the defect density, so a higher defect density will result in lower cell performance. The Frankel and

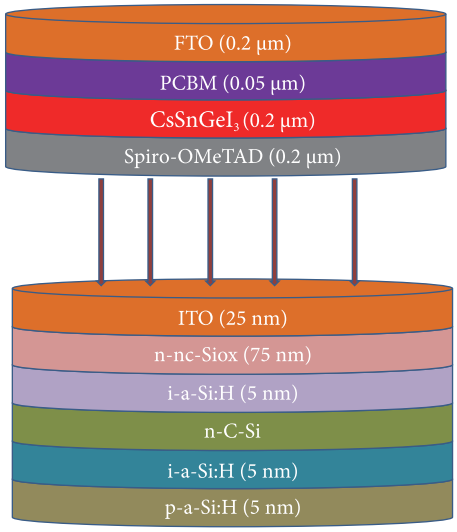

FIGURE 1: Planar structure of tandem perovskite solar cell.

Schottky defects significantly influence the open circuit voltage and diffusion length of perovskite-based solar cells. The defects introduced at the HTL/perovskite interface affect the Voc, whereas the Perovskite/ETL interface defects affect the short circuit current (J_{sc}) as given in the literature [13]. According to state-of-the-art [13], there is an adverse effect on carriers' lifetime and diffusion length, which are present in the absorber layer as the defect density increases [14, 15]. While simulating the $CsSn_{0.5}Ge_{0.5}I_3$ perovskite solar cell on SCAPS-1D, further optimization is possible by analyzing all structural parameters involved in their operation.

The proposed work simulates the cell using SCAPS-1D (created at the University of Gent) [16]. The simulation of the above device is done under steady-state conditions, and various one-dimensional equations for semiconductors, like Poisson's equation for electrons and holes, etc., are used for numerical analysis of the device. After numerical analysis, the parameters specified in SCAPS-1D are examined, including carrier density, the carrier transmit mechanism, electric field distribution, and recombination of charges.

The proposed tandem solar cell's electrical properties (electrons and holes) modeling considers Poisson's Equation (1). Equations (2) and (3) represent the continuity equations for electrons and holes, and the carrier transport equations for electrons and holes are described by Equations (4) and (5). The correlation between ρ (space charge density) and E (electric field) of the p–n junction is given below [17].

$$\frac{\partial}{\partial x}\left(\varepsilon_0 \varepsilon \frac{\partial \psi}{\partial x}\right) = -q(p - n + N_D^+ - N_A^- + p_t - n_t). \tag{1}$$

$$\frac{\partial J_n}{\partial x} - U_n + G = \frac{\partial n}{\partial t}. \tag{2}$$

$$\frac{\partial J_p}{\partial x} - U_p + G = \frac{\partial p}{\partial t}. \tag{3}$$

$$J_n = D_n \frac{d_n}{d_x} + \mu_n n \frac{d_\phi}{d_x}. \quad (4)$$

$$J_p = D_p \frac{d_p}{d_x} + \mu_n p \frac{d_\phi}{d_x}. \quad (5)$$

2. Materials and Methods

The planar structure of the monolithic PSVK/silicon tandem solar cell proposed in this paper is shown in Figure 1. The top cell of this device is made up of wide bandgap (1.5 eV) lead-free perovskite material. Different layers involved in designing the top cell are FTO, PCBM (ETL), CsSnGeI3 (perovskite layer), and spiro-OMeTAD (HTL). The critical materials used in creating these layers were taken from work published in [1, 18]. The bottom cell comprises a narrow crystalline silicon bandgap (1.12 eV). The construction of the bottom cell is done in such a manner that it behaves as a heterojunction with an intrinsic thin layer (HIT). As the perovskite material's molecular structure is ABX_3, we can alter its properties by changing the absorber layer's composition, which will directly affect the *B*—*X* bond, and the change in the composition of the halide will also change the material's properties. By doing so, the material's bandgap and even electron affinity change [12]. The properties of the material used in designing the tandem solar cells are controlled by using the SCAPS-1D simulator as described in the state-of-the-art [11, 13, 19–22]. The proposed work analyzes the PVSK/silicon tandem solar cell properties using the SCAPS-1D simulator. Most SCAPS-1D studies assume ideal perovskite/transport interfaces. In this work, we explicitly model interface defect states and their influence on carrier recombination in a Pb-free perovskite/silicon tandem. Also, inverted or bifacial tandem structures (e.g., perovskite-bottom, Si-top, etc.) are modeled in this work. The critical parameters for each of the given layers in the proposed device are shown in Table 1. Some of the parameters involved in the simulation of tandem solar cells, which are not depicted in the table, are the electron and hole cross-section value used, which was 1×10^{19} cm^{-2}. The defect level is also essential when simulating the device through SCAPS-1D. As shown in [26], an average shift of 0.2 eV in the defect levels was obtained from properly aligned total energy differences regardless of their bandgap. The characteristic energy at the bandgap center is 0.1 eV in terms of the neutral Gaussian distribution function for defect levels [27]. In the proposed work, neutral defects are used in the simulation, and the interface defects have a total density of 1×1017 cm^{-3}. The reference energy is 0.6 eV above the maximum potential energy level. The details of all the interface defects introduced in the top and bottom cells are shown in Table 2. However, owing to the limitations of the SCAPS-1D simulator, an ideal tunnel junction without optoelectrical losses is assumed between the top and bottom subcells. To perform the study of tandem design, both the cells are simulated independently; however, with different illumination spectra, the same approach is widely adopted for reporting simulation analysis of tandem design using the SCAPS-1D simulation tool. The top cell is illuminated under the standard AM1.5 spectrum, whereas the filtered spectrum by the top cell is used to simulate the bottom cell, followed by the current matching technique to finalize the tandem device. The interfacial reflection losses are ignored.

3. Results and Discussion

Section 3 discusses the results obtained in detail; broadly, it is divided into two subsections. Section 3.1 discusses calibration and simulation of the standalone top (1.5 eV) and bottom cell (1.12 eV). In Section 3.2, the performance analysis of proposed cells is done.

3.1. PVSK–Based 1.5 eV Top Cell and 1.12 eV Bottom Celloptimisation in a Stand-Alone Condition. Section 3.1 discusses the calibration of the simulated device. The results obtained by fabricating cells, as published in the literature [29], are used to get the calibrated results in the proposed work. In this process, the parameters like J_{sc} (current density) and V_{oc} (open circuit voltage) for both the cells in standalone condition are determined, as depicted in Figure 2. The graph shown in Figure 2, also known as the *J*–*V* curve, demonstrates how the current density and voltage vary when the device is illuminated by the AMI.5 spectrum. After analyzing the graph, the value of short circuit current density, that is, J_{sc}, is 18.1 mA cm^{-2} for the top cell and 32.5 mA cm^{-2} for the bottom cell. Similarly, open circuit voltage, that is, V_{oc} for the top and bottom cells, is 600 and 599 mV, respectively.

Both the cells are optimized independently before integrating into a tandem configuration. The optimization process contains the illumination of cells with the AMI.5 solar spectrum. The spectrum $s(\lambda)$ is transmitted for varying thicknesses of the absorber layer and different absorption coefficients, and the device is analyzed for this transmission. In the proposed work, the top cell is simulated by changing the width of absorber layers from 80 to 300 nm. In this process, the width of the remaining layers is unchanged, that is, they are maintained at the same level. Figure 3a depicts the top cells' filtered spectrum with varying thicknesses of absorber layers. The analysis of the graph shows that as the width of the absorber layer increases beyond 800 nm wavelength, the power of the filtered spectrum keeps decreasing. The width of the top cell directly affects the optical path length, which is the distance light travels within the cell. By increasing the width, light has a longer path to travel, increasing the likelihood of absorption by the cell material. An optimal width ensures that the cell is thick enough to absorb light effectively while still allowing sufficient light to reach the bottom cell in a tandem setup. For specific wavelengths, especially those where the absorption coefficient of the material is lower, a longer optical path allows more photons to be absorbed rather than passing through the cell without interaction. The reason for reduced power is higher absorption in thicker layers. Similarly, the bottom cell is also fed with the solar spectrum, and after this, the optical coupling of both cells is done. In optical coupling, the photons from both the cells are coupled together. The transmitted spectrum for the proposed device shown in Figure 3a demonstrates that for thin absorber layers like 80 nm, a greater amount of photocurrent is transmitted to the bottom subcells, as the amount of photocurrent absorbed is less in these layers, but as the thickness of the

Table 1: The different material and their parameters used in the simulation.

Parameters	FTO [1]	PCBM [23]	CsSnGeI3	Spiro-OMeTAD [6]	ITO [24]	n-nc-SiOx [5]	i-a-Si:H [5, 25]	C—Si [8]	p-a-Si:H [25]
Thickness (nm)	200	50	200 Variable	200	25	75	5	Variable	5
Bandgap energy, E_g (eV)	3.2	2.0	1.5	2.9	3.72	1.40	1.72	1.120	1.72
Electron affinity, χ (eV)	4.4	3.9	3.9	2.2	3.6	3.940	3.80	4.05	3.80
Relative dielectric permittivity, ε_r	9.0	9.0	28.0	3	9.4	11.9	11.9	11.90	11.9
CB density of states, N_C (cm^{-3})	2.2×10^{18}	1.7×10^{19}	1×10^{19}	1.8×10^{18}	2.2×10^{19}	2.8×10^{19}	2.5×10^{20}	2.80×10^{19}	2.5×10^{20}
VB density of states, N_V (cm^{-3})	1.8×10^{19}	1.2×10^{19}	1×10^{19}	1.8×10^{18}	1.8×10^{19}	1.4×10^{19}	2.5×10^{20}	1.04×10^{19}	2.5×10^{20}
Mobility of electron, μ_e (cm^2/Vs)	90	2×10^{-1}	974	2×10^{-4}	1×10^{1}	1.4×10^{3}	20	1.4×10^{3}	20
Mobility of hole, μ_h (cm^2/Vs)	90	2×10^{-1}	213	2×10^{-4}	1×10^{1}	4.5×10^{2}	5	4.5×10^{2}	5
Donor density, N_D (cm^{-3})	2×10^{19}	1×10^{17}	0	0	1×10^{19}	1×10^{20}	0	5×10^{16}	0
Acceptor density, N_A (cm^{-3})	0	0	1×10^{14}	1.3×10^{18}	—	—	0	—	1×10^{20}
Defect density, N_t (cm^{-3})	1×10^{15}	1×10^{17}	1×10^{17}	1×10^{14}	—	—	—	—	—

Table 2: Interface defects [28].

Parameters	Interface						
	Defect type	σ_n (cm^2)	σ_p (cm^2)	Dist.	Reference level	Energy level (eV)	Total density (cm^{-2})
SnO_2/PCBM	N	1×10^{15}	1×10^{-15}	S	Above 0.6	0.6	1×10^{14}
PCBM/PVK	N	1×10^{-15}	1×10^{-15}	S	Above 0.6	0.6	1×10^{14}
PVK/CuSCN	N	1×10^{-15}	1×10^{-15}	S	Above 0.6	0.6	1×10^{14}
i-a-Si:H/nc-SiOx	N	1×10^{-15}	1×10^{-15}	S	Above 0.6	0.6	1×10^{1}
n-C-Si/i-a-Si:H	N	1×10^{-15}	1×10^{-15}	S	Above 0.6	0.6	1×10^{1}
i-a-Si:H/n-C-Si:H	N	1×10^{-15}	1×10^{-15}	S	Above 0.6	0.6	1×10^{1}
p-a-Si:H/i-a-Si:H	N	1×10^{-19}	1×10^{-19}	S	Above 0.6	0.6	1×10^{1}
	Defect 1			Defect 2		Defect 3	
i-a-Si:H	Charge type: amphoteric: [+/0, 0/−] N_t: Uniform 8×10^{16} cm^{-3} Eg D, Gauss; E_t = [0.70; 0.50] eV below E_c			Charge type: acceptor: [0/−] N_t: Uniform 10^{16} cm^{-3} Eg D, CB tail; E_t = 0.01 eV below E_C		Charge type: donor: [+/0] N_t: Uniform 10^{16} cm^{-3} Eg D, VB tail; E_t = 0.01 eV above E_V	
p-a-Si:H	Amphoteric: [+/0, 0/−] N_t: Uniform 8×10^{14} cm^{-3} Eg D, Gauss; E_t = [0.70; 0.50] eV below E_c			Charge type: acceptor: [0/−] N_t: Uniform 10^{15} cm^{-3} Eg D, CB tail; E_t = 0.01 eV below E_C		Charge type: donor: [+/0] N_t: Uniform 8×10^{16} cm^{-3} Eg D, VB tail; E_t = 0.01 eV above E_V	

Note: N is for neutral defect. S is for single distance.
Abbreviation: Eg D, energy distribution.

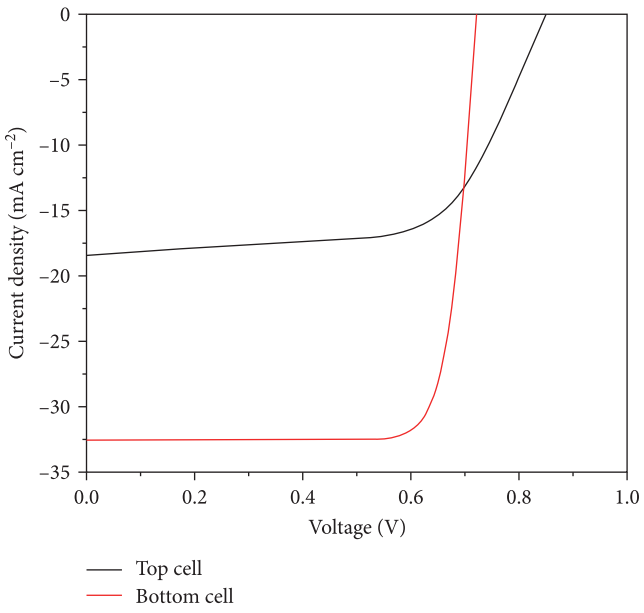

Figure 2: Current density (J)-voltage (V) curve for illuminated cells.

absorber layer increases, the transmitted photocurrent gets reduced.

3.2. Analysis of PVSK–Si Tandem Solar Cell. This section analyzes the proposed PVSK/Si tandem solar cell. The tandem cell is constructed by integrating the standalone top and bottom cells together. The behavior of the proposed cell will be the same as that of two diodes connected in series, and because of this property, the amount of current flowing through each cell should be the same. Thus, the resultant device acts as two terminal monolithic tandem solar cells. The overall voltage drop across this device can be determined by adding the voltage drop across individual cells. Calculating short circuit current (J_{sc}) is an essential parameter in the resultant device. A tandem device consists of top and bottom cells, where the limiting cell for current density will be the cell with lower J_{sc}. In the proposed device, the top cell has a lower J_{sc} value, so its value will be taken as the short circuit current for the resultant device. To calculate the open circuit voltage V_{oc} of the resultant device, we will add the individual voltages of the top and bottom cells, respectively. The amount of J_{sc} (short circuit current) flowing in both the cells of the tandem device should be the same; to achieve this, the width of both the cells is optimized accordingly, and the utilization of the same tunnel recombination junctions is done [23].

The width of the top cell plays a significant role in deciding the overall J_{sc} of the tandem device; the short-circuit current decreases by increasing the thickness beyond the ideal range. This happens because of parasitic absorption in the top cell and decreased optical coupling in the bottom cell. Similarly, if the width of the top cell is reduced below the optimum level, the J_{sc} value of the device will increase because of the reduction in the top cell's absorption.

The proposed device is constructed by stacking together two subcells, so the critical factor is the matching of current between them, which illuminates them with a computed filtered spectrum. To achieve this, we vary the top cell thickness from 80 to 300 nm, as illustrated in Figure 3b. After this, the bottom cell is illuminated with 11 filtered spectrums, as shown in Figure 3a, and the PV parameters for the proposed cell are calculated. The bottom cells' absorption layers were varied from 80 to 300 nm in 10 equal steps. Figure 3b shows that the top cell J_{sc} values under the filtered spectrum are used to evaluate the current matching condition. To achieve this current matching condition, the top cell thickness is 200 nm, and

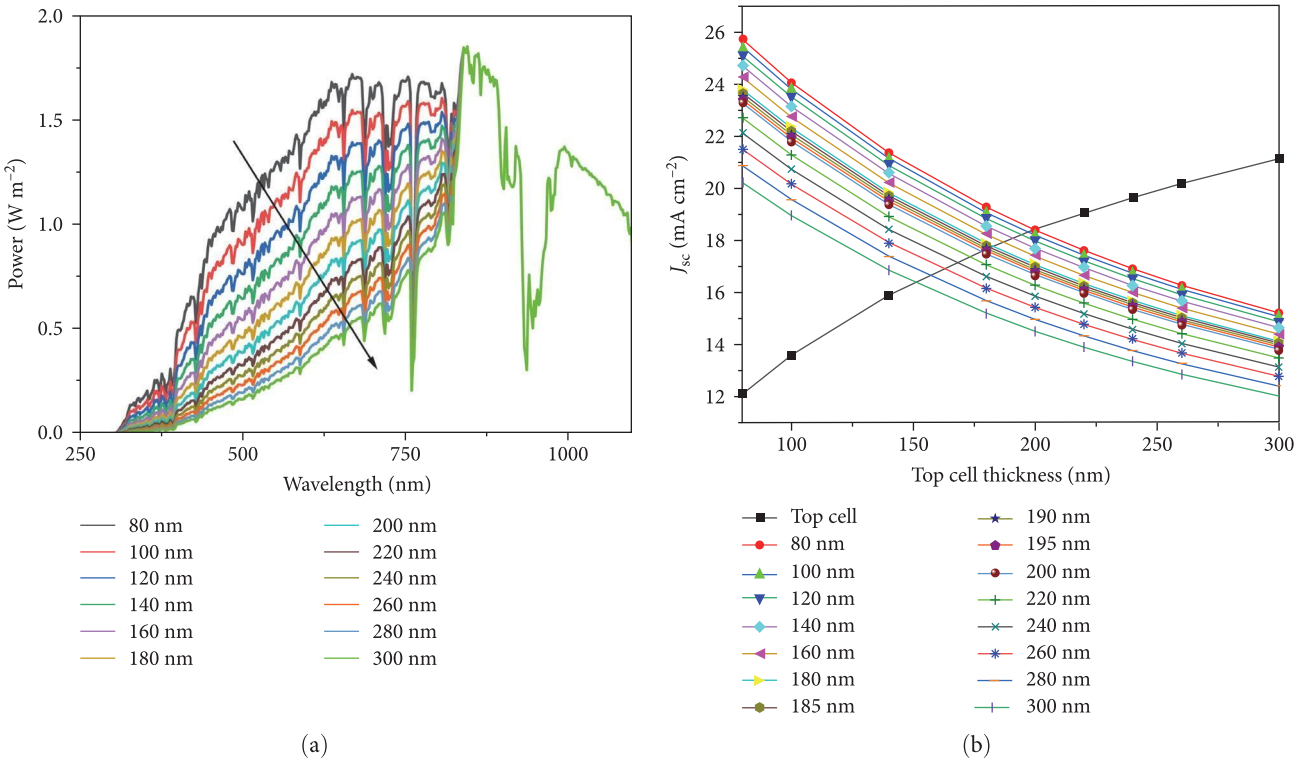

FIGURE 3: (a) Power is obtained by transmitting a spectrum to the top cell at different thicknesses, from 80 to 300 nm. (b) Short circuit current (J_{sc}) for individual top and bottom cells of varying thickness (80–300 nm). The curve has been used to obtain the current matching condition.

the bottom is 100 nm. The J_{sc} for the top cell is 18.35 mA cm^{-2}, and that for the bottom cell is 32.52 mA cm^{-2}. As the top cell acts as the current-limiting cell, the J_{sc} of the tandem device is 18.34 mA cm^{-2}, approximately equal to the top cell J_{sc}.

The current–voltage curve for the tandem solar cell is obtained by calculating Voc for both the top and bottom cells at equal current points [30, 31]. Figure 4a shows the *J–V* curve of standalone top and bottom cells; the figure also depicts the *J–V* curve for tandem devices from which the current matching condition can be obtained. Figure 4 is obtained at the initial stage when no filtered spectrum is fed to these cells. After the top, bottom and tandem cells are illuminated with filtered spectrum, the *J–V* curve is shown in Figure 4b. The figure depicts that the top cell has a large V_{oc}, as it has a large bandgap, but the short circuit current (J_{sc}) is lower than the bottom cell. The tandem *J–V* curve does not originate from the origin because the series-connected top and bottom subcells have different dark current characteristics, and the recombination layer enforces current continuity, leading to an offset even before illumination. The PV parameters obtained by the simulation of standalone top and bottom cells and tandem devices are mentioned in Table 3. The proposed tandem device shows comparable efficiency with the existing literature [32, 33]. By analyzing the parameters, we concluded that V_{oc} is the sum of voltage drops at the top and bottom cells for the proposed tandem device. The V_{oc} for the tandem configuration is 1.576 V. Proper band alignment between the top and bottom cells in the tandem configuration ensures efficient charge separation and minimizes potential barriers to charge transport. This alignment helps maintain a high V_{oc} by facilitating efficient electron and hole extraction. Choosing high-quality semiconductor materials for the top and bottom cells is crucial in achieving a high V_{oc}. J_{sc} is the same as the current density of the top cell, which acts as a limiting cell, and PCE is much higher than the efficiency of the top and bottom cells individually. The efficiency of top, bottom, and tandem solar cells—when discussed in terms of material and design (bandgap, current matching, etc.)—is not related to R_s and R_{sh}, because those resistances are parasitic electrical losses, not fundamental material or optical properties.

4. Conclusion

This paper proposes a lead-free monolithic perovskite/silicon tandem solar cell. The advantage of tandem devices over single-junction cells is high PEC, which was the motivating factor for implementing tandem solar cells. The proposed cell is constructed by integrating a wide bandgap top and narrow bandgap bottom cell, and due to different bandgaps, the two subcells will consume different solar spectrum bands, which results in a high rate of light conversion. The optimization of the tandem device having an n-i-p configuration is done by a solar cell capacitance simulator. Because of its planar structure, the current should be matched between the top and bottom cells in the proposed two-terminal tandem solar cell. The absorber layers' thickness varies to achieve the current matching condition, and the solar spectrum is fed to both layers. In this work, the optimized thickness of the top and bottom cells for current matching is 100 and 200 nm, respectively, at the matched current: $J_{sc} = 18.34$ mA cm^{-2}. The efficiency of standalone

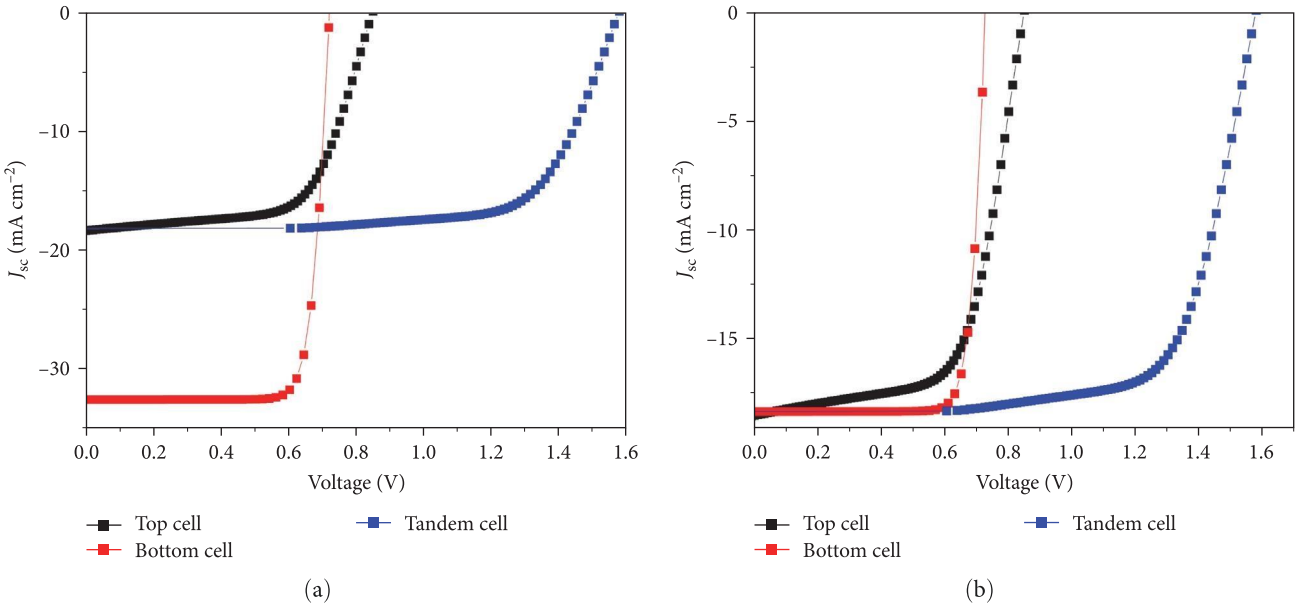

FIGURE 4: (a) J_{sc}–V curve for perovskite (top) and silicon (bottom) cell and tandem cell before illumination with solar spectrum. (b) J_{sc}–V curve for a perovskite (top), silicon (bottom), and tandem cell after illumination with the solar spectrum.

TABLE 3: The simulated parameters of standalone top, bottom, and proposed tandem solar cell.

Cell	Voc (V)	J_{sc} (mA cm^{-2})	FF (%)	PCE (%)
Top cell	0.8494	18.35	63.91	9.96
Bottom cell	0.7213	32.52	82.03	19.25
Tandem cell	1.576	18.34	90	25.80

top and bottom cells is 9.96% and 19.25%, respectively, while the efficiency of tandem solar cells has increased to 25.8%. Other parameters of the simulated tandem device are $V_{oc} = 1.576$ V and fill factor (FF) = 90%. The architecture of the tandem solar cell was carefully designed to ensure efficient charge transport and collection. This includes optimizing layer thicknesses and doping concentrations to balance carrier generation and extraction. The high % FF of 90% results from using high-quality materials and optimized device architecture. The PVSK/Si described here offers a path for continued development in lead-free, inexpensive, and highly efficient energy conversion systems. The novelty of this work lies in the simulation-based design of a highly efficient, lead-free monolithic perovskite/silicon tandem solar cell using SCAPS-1D, combining environmentally safe materials with advanced device architecture to achieve superior performance while addressing toxicity concerns of conventional perovskites.

Data Availability Statement

The data that support the findings of this study are available upon request from the corresponding author. The data are not publicly available due to privacy or ethical restrictions.

Conflicts of Interest

The authors declare no conflicts of interest.

Funding

No Funding is received for this research work.

References

[1] A. Kojima, K. Teshima, Y. Shirai, and T. Miyasaka, "Organometal Halide Perovskites as Visible-Light Sensitizers for Photovoltaic Cells," *Journal of the American Chemical Society* 131, no. 17 (2009): 6050-6051.

[2] M. A. Nalianya, C. Awino, H. Barasa, et al., "Numerical Study of Lead Free CsSn0.5Ge0.5I3 Perovskite Solar Cell by SCAPS-1D," *Optik* 248 (2021): 168060.

[3] N. J. Jeon, H. Na, E. H. Jung, et al., "A Fluorene-Terminated Hole-Transporting Material for Highly Efficient and Stable Perovskite Solar Cells," *Nature Energy* 3, no. 8 (2018): 682–689.

[4] M. A. Green, A. Ho-Baillie, and H. J. Snaith, "The Emergence of Perovskite Solar Cells," *Nature Photonics* 8, no. 7 (2014): 506–514.

[5] F. Hao, C. C. Stoumpos, D. H. Cao, R. P. H. Chang, and M. G. Kanatzidis, "Lead-Free Solid-State Organic–Inorganic Halide Perovskite Solar Cells," *Nature Photonics* 8 (2014): 489–494.

[6] B. Wu, Y. Zhou, G. Xing, et al., "Long Minority-Carrier Diffusion Length and Low Surface-Recombination Velocity in Inorganic Lead-Free $CsSnI_3$ Perovskite Crystal for Solar Cells," *Advanced Functional Materials* 27, no. 7 (2017): 1604818.

[7] M. Chen, M. G. Ju, H. F. Garces, et al., "Highly Stable and Efficient All-Inorganic Lead-Free Perovskite Solar Cells With Native-Oxide Passivation," *Nature Communications* 10, no. 16 (2019): 16.

[8] H. Sabbah, "Numerical Simulation of 30% Efficient Lead-Free Perovskite CsSnGeI3-Based Solar Cells," *Materials* 15, no. 9 (2022): 3229.

[9] L. Lang, J. H. Yang, H. R. Liu, H. J. Xiang, and X. G. Gong, "First-Principles Study on the Electronic and Optical Properties of Cubic ABX3 Halide Perovskites," *Physics Letters A* 378 (2014): 290–293.
[10] M. Burgelman, K. Decock, A. Niemegeers, J. Verschraegen, and S. Degrave, "SCAPS Manual, Version," (2018).
[11] T. Minemoto and M. Murata, "Impact of Work Function of Back Contact of Perovskite Solar Cells Without Hole Transport Material Analyzed by Device Simulation," *Applied Physics* 14 (2014): 1428–1433.
[12] G. C. Xing, N. Mathews, S. Y. Sun, et al., "Long-Range Balanced Electron- and Hole-Transport Lengths in Organic- Inorganic CH3NH3PbI3," *Science* 342, no. 6156 (2013): 344–347.
[13] Q. Zhou, D. Jiao, K. Fu, et al., "Two-Dimensional Device Modeling of CH3NH3PbI3 Based Planar Heterojunction Perovskite Solar Cells," *Solar Energy* 123 (2016): 51–56.
[14] S. Chauhan and R. Singh, "Investigation of 2T Pb-Free Wide Bandgap Perovskite/c-Si Tandem Device Through Simulation by SCAPS-1D." *Sādhanā* 48 (2023): 40.
[15] M. Dahmardeh and M. Saadat, "Exploring the Potential of Standalone and Tandem Solar Cells With Sb_2S_3 and Sb_2Se_3 Absorbers: A Simulation Study," *Scientific Reports* 13, no. 1 (2023): 22632.
[16] M. Burgelman, P. Nollet, and S. Degrave, "Modelling Polycrystalline Semiconductor Solar Cells," *Thin Solid Films* 361-362 (2000): 527–532.
[17] G. Jiménez-Castillo, A. J. Martínez-Calahorro, C. Rus-Casas, A. Snytko, and F. J. Muñoz-Rodríguez, "Performance Analysis Indices for Rooftop Solar Photovoltaic System," *IEEE Latin America Transactions* 21, no. 9 (2023): 999–1006.
[18] J. Wei, Q. Xiong, S. Mahpeykar, and X. Wang, "Numerical Study of Complementary Nanostructures for Light Trapping in Colloidal Quantum Dot Solar Cells," *Nanomaterials* 6, no. 4 (2016): 1601130.
[19] L. kegelmann, C. M. Wolf, C. Awino, et al., "It Takes Two to Tango—Double-Layer Selective Contacts in Perovskite Solar Cells for Improved Device Performance and Reduced Hysteresis," *ACS Applied Materials & Interfaces* 9, no. 20 (2017): 17245–17255.
[20] M. I. Hossain, F. H. Alharbi, and N. Tabet, "Copper Oxide as Inorganic Hole Transport Material for Lead Halide Perovskite Based Solar Cells," *Solar Energy* 120 (2015): 370–380.
[21] A. Alsalme and H. Alsaeedi, "Twenty-Two Percent Efficient Pb-Free All-Perovskite Tandem Solar Cells Using SCAPS-1D," *Nanomaterials* 13, no. 1 (2023): 1–11.
[22] L. Duan, S. P. Phang, D. Yan, et al., "Over 29%-Efficient, Stable n-i–p Monolithic Perovskite/Silicon Tandem Solar Cells Based on Double-Sided Poly-Si/SiO_2 Passivating Contact Silicon Cells," *Journal of Materials Chemistry A* 12, no. 31 (2024): 20006–20016.
[23] B. Chen, Z. Yu, K. Liu, et al., "Grain Engineering for Perovskite/Silicon Monolithic Tandem Solar Cells With Efficiency of 25.4%, *Joule* 3, no. 1 (2019): 177–190.
[24] S. Kazim, M. K. Nazeeruddin, M. Grätzel, and S. Ahmad, "Perovskite as Light Harvester: A Game Changer in Photovoltaics," *Angewandte Chemie International Edition* 53, no. 11 (2014): 2812–2824.
[25] T. Minemoto and M. Murata, "Theoretical Analysis on Effect of Band Offsets in Perovskite Solar Cells," *Solar Energy Materials and Solar Cells* 133 (2015): 8–14.
[26] A. Alkauskas, P. Broqvist, and A. Pasquarello, "Defect Energy Levels in Density Functional Calculations: Alignment and Band Gap Problem," *Physical Review Letters* 101, no. 4 (2008): 046405.
[27] A. Zekry, I. Yahyaoui, and F. Tadeo, "2019 10th International Renewable Energy Congress (IREC)," , (IEEE: 1–6.
[28] S. Chauhan and R. Singh, "Analysis of Absorber Layer for Wide-Bandgap Double Perovskite Solar Cell Using SCAPS-1D," *Materials Today: Proceedings* (2023).
[29] G. E. Eperon, T. Leijtens, K. A. Bush, et al., "Perovskite-Perovskite Tandem Photovoltaics With Optimized Band Gaps," *Science* 354, no. 6314 (2016): 861–865.
[30] J. Burdick and T. Glatfelter, "Spectral Response and I-V Measurements of Tandem Amorphous-Silicon Alloy Solar Cells," *Solar Cells* 18, no. 3 (1986): 301–314.
[31] K. Kim, J. Gwak, S. K. Ahn, et al., "Simulations of Chalcopyrite/c-Si Tandem Cells Using SCAPS-1D," *Solar Energy* 145 (2017): 52–58.
[32] K. Amri, R. Belghouthi, M. Aillerie, and R. Gharbi, "Device Optimization of a Lead-Free Perovskite/Silicon Tandem Solar Cell With 24.4% Power Conversion Efficiency," *Energies* 14 (2021): 3383.
[33] N. Shrivastav, J. Madan, and R. Pandey, "Optimizing Tandem Solar Cells Efficiency Through Current Matching Technique in Lead-Free Perovskite/c-Si and Lead-Free Perovskite/CIGS Absorbers," *Indian Journal of Physics* (2024).